

# Quantum-assisted distortion-free audio signal sensing

**Chen Zhang** (✉ [chen.zhang@pi3.uni-stuttgart.de](mailto:chen.zhang@pi3.uni-stuttgart.de))

University of Stuttgart

**Durga Dasari**

University of Stuttgart

**Matthias Widmann**

University of Stuttgart

**Jonas Meinel**

University of Stuttgart <https://orcid.org/0000-0003-4040-8361>

**Vadim Vorobyov**

University of Stuttgart

**Polina Kapitanova**

ITMO University

**Elizaveta Nenasheva**

Giricond Research Institute, Ceramics Co., Ltd.

**Kazuo Nakamura**

Tokyo Gas Co., Ltd. <https://orcid.org/0000-0002-3412-834X>

**Hitoshi Sumiya**

Sumitomo Electric Industries

**Shinobu Onoda**

National Institutes for Quantum Science and Technology <https://orcid.org/0000-0003-1425-0708>

**Junichi Isoya**

University of Tsukuba <https://orcid.org/0000-0002-9598-625X>

**Jörg Wrachtrup**

University of Stuttgart

---

## Article

**Keywords:** Quantum sensors, metrology, audio signal sensing

**Posted Date:** November 19th, 2021

**DOI:** <https://doi.org/10.21203/rs.3.rs-1068484/v1>

**License:**  This work is licensed under a Creative Commons Attribution 4.0 International License.

[Read Full License](#)

---

**Version of Record:** A version of this preprint was published at Nature Communications on August 8th, 2022. See the published version at <https://doi.org/10.1038/s41467-022-32150-1>.

# Quantum-assisted distortion-free audio signal sensing

Chen Zhang,<sup>1,\*</sup> Durga Dasari,<sup>1,†</sup> Matthias Widmann,<sup>1</sup> Jonas Meinel,<sup>1</sup> Vadim Vorobyov,<sup>1</sup> Polina Kapitanova,<sup>2</sup> Elizaveta Nenasheva,<sup>3</sup> Kazuo Nakamura,<sup>4</sup> Hitoshi Sumiya,<sup>5</sup> Shinobu Onoda,<sup>6</sup> Junichi Isoya,<sup>7</sup> and Jörg Wrachtrup<sup>1</sup>

<sup>1</sup>*3rd Institute of Physics, University of Stuttgart,  
Pfaffenwaldring 57, Stuttgart 70569, Germany*

<sup>2</sup>*Department of Physics and Engineering,  
ITMO University, Saint Petersburg 197101, Russia*

<sup>3</sup>*Giricond Research Institute, Ceramics Co. Ltd., Saint Petersburg 194223, Russia*

<sup>4</sup>*Hydrogen and Carbon Management Technology Section,  
Hydrogen and Carbon Management Technology Strategy Department,  
Tokyo Gas Co. Ltd., Yokohama 230-0045, Japan*

<sup>5</sup>*Advanced Materials Laboratory, Sumitomo Electric Industries Ltd., Itami 664-0016, Japan*

<sup>6</sup>*Takasaki Advanced Radiation Research Institute,  
National Institutes for Quantum Science and Technology, Takasaki 370-1292, Japan*

<sup>7</sup>*Faculty of Pure and Applied Sciences,  
University of Tsukuba, Tsukuba 305-8573, Japan*

# Abstract

Quantum sensors are keeping the cutting-edge sensitivities in metrology. However, for high-sensitive measurements of arbitrary signals, limitations in linear dynamic range could introduce distortions when sensing the frequency, magnitude and phase of unknown signals. Here, we overcome these limitations with advanced sensing protocol that combines quantum phase-sensitive detection with the heterodyne readout. We present theoretical and experimental investigations using nitrogen-vacancy centers in diamond, showing the ability to sense audio signals with a 98 dB linear dynamic range, a 31 pT/Hz<sup>1/2</sup> sensitivity, and arbitrary frequency resolution. Further, we perform the quantum assisted distortion free audio signal (melody piece, speech) sensing with high fidelity. The methods developed here could broaden the horizon for quantum sensors towards applications in telecommunication, where high-fidelity and low-distortion at multiple frequency bands within small sensing volumes are required.

## 18 I. INTRODUCTION

19 Quantum sensors are setting new frontiers of sensing techniques with their extraordinary  
20 performances in sensitivity and stability [1–5]. These techniques rely on either measuring  
21 the line-shift of spin or atomic transition frequencies or reading out the relative populations  
22 of the occupied energy levels using interferometric methods [6, 7]. In most cases, there  
23 are trade-off relations between the sensitivity and other features in metrology [8]. For  
24 example, a high-sensitive measurement acquired by detecting the transition line shift requires  
25 a narrow linewidth, which, on the other hand, will limit the dynamic range. Interferometric  
26 measurements detect a sinusoidal response, and linearity is only achieved when the phase  
27 signal is in a small dynamic range. It sets a massive limitation on the sensitivity when  
28 sensing an unknown signal that gets measured beyond this linear regime, for example, when  
29 the working point of the sensor is at the maxima or minima of the sinusoidal signal response.  
30 Thus, it becomes a bottleneck for high sensitivity measurements that are required in many  
31 cutting-edge applications. Operating within the linear dynamic range (LDR) can be crucial  
32 for reconstructing unknown signals. One way to directly extract the phase factor, which is

---

\* c.zhang@pi3.uni-stuttgart.de

† d.dasari@pi3.uni-stuttgart.de

33 linear to the physical quantity to be detected, is to use phase-sensitive detection known as the  
34 classical lock-in technique. In this work, using a modified sensing scheme that introduces  
35 an external readout phase modulation, we acquire the target quantum phase signal after  
36 demodulation. Therefore, the LDR is no longer limited to the small-angle approximation.  
37 Hence our method combines large dynamic range with maximum sensitivity.

38 Nitrogen-vacancy (NV) centers in diamond have been at the forefront in performing  
39 high-sensitive measurements of various physical quantities, viz., magnetic and electric field,  
40 temperature, and strain distributions internal and external to diamond [9–13]. The NV  
41 magnetometry has been performed under bias fields ranging from zero-field to a few Tesla,  
42 and for sensing signals with frequencies ranging from DC to a few GHz [14–17]. While  
43 dynamical-decoupling techniques are usually employed for high sensitivity [9, 18, 19], arbi-  
44 trary frequency resolution can be achieved with the quantum heterodyne (Q-dyne) detection  
45 [20, 21]. However, both methods suffer from a limited LDR when they are applied to measure  
46 arbitrary signals.

47 For high dynamic range measurements, a closed-loop frequency-locking scheme together  
48 with optically detected magnetic resonance (ODMR) can be used to track resonance fre-  
49 quency shifts [22]. However, this scheme cannot be used for ac field measurements in combi-  
50 nation with interferometric methods, if the signal frequency is higher than the readout sam-  
51 pling frequency. Phase-estimation algorithms can effectively improve the LDR in Ramsey  
52 measurements by varying the sequence with adaptive feedback schemes [23, 24]. However,  
53 for the case of ac sensing schemes e.g. Hahn-echo, as varying the sequence itself will change  
54 the sensor response to the ac signals, such methods become less applicable. Therefore, a  
55 technique is still missing, that addresses the LDR while maintaining high sensitivity and  
56 frequency resolution, for example, in sensing arbitrary radio-frequency fields within a broad  
57 bandwidth.

58 Sensing radio-frequency signals by electric-field sensors, either conventional electronic  
59 receivers or the Rydberg atom sensors, need antennas to collect and guide the electric  
60 signals towards the sensors [25–28]. Although the receivers can be highly integrated, the  
61 dimension of antennas can scale to meters due to the signal wavelength. The size becomes  
62 critical when there is limited space for the sensor, for example, in a satellite. In this regard,  
63 quantum magnetometers can be very attractive due to their small sensing volume and high  
64 sensitivity [29]. A flux concentrator can be used as a substitute to conventional antennas

65 for obtaining high signal gain. Independent of the signal wavelength, the dimensions of such  
66 flux concentrators can be as small as a few centimeters [30, 31].

67 In this paper, we demonstrate quantum-assisted distortion-free audio signal sensing with  
68 NV center ensembles in diamond using the quantum-phase-sensitive detection (QPSD) tech-  
69 nique combined with heterodyne readout. Firstly, we introduce the QPSD technique, which  
70 can provide an extended LDR in interferometry measurements by using two synchronized  
71 driving fields. Then, we present the heterodyne readout, which can interpret e.g. ac signals  
72 to get frequency information. Taking advantage of the bandwidth of the Hahn-echo sequence  
73 and the frequency comb induced by the continuous sampling, we demonstrate measurements  
74 of audio signals around 10 kHz, beyond the coherence limit without losing sensitivity. Fi-  
75 nally, we present arbitrary audio signal measurements with a LDR of 98 dB at a sensitivity  
76 of 31 pT/Hz<sup>1/2</sup>. A piece of melody and a speech are encoded as magnetic field signals and  
77 measured by the NV magnetometer. By using the sensor as a quantum radio, we demon-  
78 strate the application potentials for areas such as quantum-assisted telecommunication and  
79 unknown signal exploration.

## 80 II. RESULTS

### 81 A. Quantum Phase Sensitive Detection

82 In interferometric measurements, the quantum phase to be detected is usually converted  
83 to a quantum state population difference, resulting in a sinusoid readout [9]. A way to  
84 extract the phase factor from the sinusoidal readout is to modulate the phase with a specific  
85 frequency and perform phase-sensitive modulation. Such a quantum phase modulation can  
86 be introduced by using the difference between the quantum phase of the sensor to an ex-  
87 ternal oscillator. The Q-dyne method uses such a strategy for resolving frequency of signals  
88 better than the relaxation time of the sensor, as shown in Fig. 1a [20, 21]. However, it  
89 cannot be used for phase-sensitive detection because the Q-dyne frequency is also what to  
90 be resolved and an extra modulation is still needed [21]. Another way to introduce such a  
91 phase modulation is to use the frequency offset between two different driving fields of the  
92 sensor [32, 33]. These driving fields define two rotating frames, and the evolution of the spin  
93 as seen from one rotating frame will lead to a quantum phase modulation due to the relative

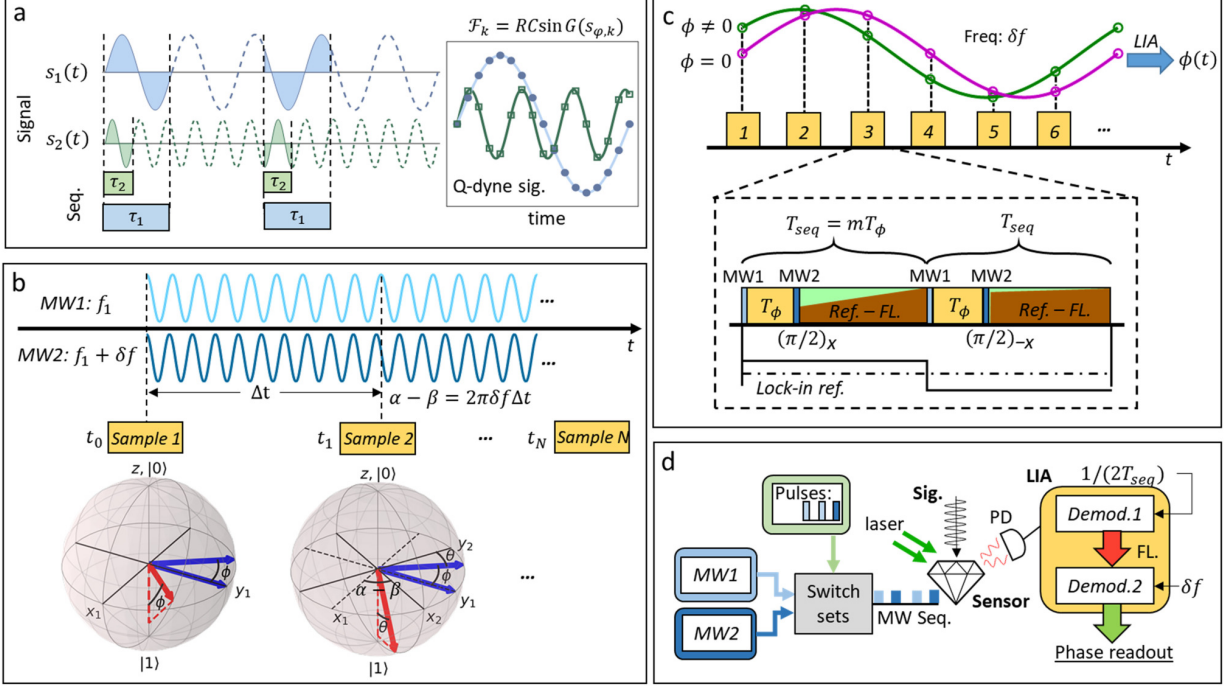


FIG. 1. Phase-sensitive NV magnetometry (a) Continuous sampling induced phase reviving signals, known as the quantum heterodyne (Q-dyne) detection. The phase reviving frequency changes with the external field and cannot be used for phase-sensitive detection. The signal responses  $G(s_{\phi}, k)$  should be small to ensure measurement linearity.  $R$  is the detected photon rate, and  $C$  is the detected signal contrast. (b) Unlike the Q-dyne detection, the quantum phase-sensitive detection (QPSD) is based on the rotating frame modulation induced by the evolving phase difference of the two driving MW fields. Two frequency-offset MWs acquire a phase difference of  $\alpha - \beta = 2\pi\delta f \Delta t$  after the sampling time interval  $\Delta t$ . In the Bloch sphere picture, it can be understood as the MW2 defined rotating frame  $x_2y_2z$  rotates with rate of  $\delta f$  referring to the MW1 defined rotating frame  $x_1y_1z$ . The acquired quantum phase is  $\theta = 2\pi\delta f \Delta t - \phi$  at sample 2. Through the quantum phase modulation, the acquired readout representing the Bloch vector projections is as shown in (c), where we present the measurements of the quantum phase  $\phi = 0$  and  $\phi \neq 0$ . By demodulating the acquired signal with a lock-in amplifier, we can get the phase values. The dashed box shows the measurement sequences we applied in experiments. Except for the last  $\pi/2$  pulse applied with MW2, all the other driving pulses are generated by MW1. The fluorescence signal is demodulated at the frequency of  $1/(2T_{seq})$  to get a fluorescence intensity readout for a sample. The QPSD readout is acquired with the demodulation at  $\delta f$ . (d) Schematic of the experiment. NV centers ensemble in diamond is used to perform the QPSD readout.

94 rotation of the two frames, i.e., rotating frame modulation. The modulation frequency only  
 95 depends on the frequency difference of the two driving fields, as shown in Fig. 1b and c.  
 96 By performing multiple measurements within a modulation cycle and upon using lock-in  
 97 detection, we will achieve phase-sensitive detection. Below we mathematically describe this  
 98 relative evolution of the sensor under such interferometric measurement with two-frequency

99 driving fields.

100 Aligning an external field  $B_0$  along the NV axis, we use the two-level subspace of the NV  
 101 ground triplet in the derivation. Thus, the Hamiltonian of the system can be written as:

$$\mathcal{H} = \omega_0 S_z + \gamma_e B_1 \cos(2\pi f_1 t + \alpha) S_x, \quad (1)$$

102 where  $\omega_0$  is the transition frequency of the two-level subspace,  $B_1$  is the oscillating magnetic  
 103 field perpendicular to the NV axis,  $f_1$  and  $\alpha$  are the frequency and phase of the driving field,  
 104 and  $\gamma_e$  is the electron gyromagnetic ratio. In the rotating frame defined by the resonance  
 105 frequency, the time-dependent Hamiltonian is

$$\mathcal{H}'_1 = \Omega_1 \cos(\delta\omega_1 + \alpha) S_x + \Omega_1 \sin(\delta\omega_1 t + \alpha) S_y, \quad (2)$$

106 where  $\delta\omega_1 = 2\pi(f_0 - f_1)$ , and  $\Omega_1 = \gamma_e B_1/2$  is the Rabi frequency introduced by MW1. In  
 107 interferometry measurements, a  $\pi/2$  pulse prepares the spin state from the polarized state to  
 108 an equalized population, and another  $\pi/2$  pulse projects the quantum phase as a population  
 109 difference after the sensing procedure. We use the second driving field, MW2, to offset the  
 110 frequency of the second  $\pi/2$  pulse.  $\delta\omega_2, \beta$  and  $\Omega_2$  are used to denote the frequency offset,  
 111 Rabi frequency, and phase of MW2. After this, the measured spin-expectation value is

$$\langle S_z \rangle = \sin \left[ \phi + \frac{\pi}{2} \left( \frac{\delta\omega_1}{\Omega_1} - \frac{\delta\omega_2}{\Omega_2} \right) + \alpha - \beta \right], \quad (3)$$

112 where  $\phi$  is the acquired quantum phase which contains the information we want to measure,  
 113 both of the MWs are near-resonant with  $\delta\omega_1 \ll \Omega_1$ ,  $\delta\omega_2 \ll \Omega_2$ . Therefore, the off-resonant  
 114 term can be neglected, and the phase difference term  $\alpha - \beta$  will evolve with time so that  
 115 there is

$$\langle S_z \rangle \approx \sin(\phi + 2\pi\delta f \cdot t), \quad (4)$$

116 where  $\delta f$  is the frequency difference of the two MWs.

117 The above result can be seen as a modulation of the rotating frame itself. As schematically  
 118 shown in Fig. 1b (left Bloch sphere), we can assume that the two driving fields have the same  
 119 phase at the duration of the second  $\pi/2$  pulse, and this defines an instantaneous rotating  
 120 frame with coordinates  $x_1 y_1 z$ . Thus, the readout is similar to that of the regular Ramsey

121 interferometry using a single driving field. After an interval of  $\Delta t$ , MW2 develops a phase  
 122 difference of  $2\pi\delta f\Delta t$ . Since the quantum phase is finally measured by MW2, the Bloch  
 123 vector rotates in the new instantaneous rotating frame with coordinates  $x_2y_2z$ , as shown in  
 124 Fig. 1b (the right Bloch sphere). The rotating frame defined by MW2 rotates continuously  
 125 around the  $z$ -axis with the frequency of  $\delta f$ . Due to this, the fluorescence readout also  
 126 modulates in a sinusoidal fashion, as shown in Fig. 1c. While the readout signal frequency  
 127 depends on  $\delta f$  and its amplitude depends on the signal contrast, the initial phase,  $\varphi$ , is  
 128 linear to the field to be measured. Through the external modulation induced by the MWs,  
 129 the working point of the sensor evolves in the entire phase range, which ensures the LDR of  
 130 the initial phase measurement covering  $[-\pi, \pi]$ . By fitting or demodulating the fluorescence  
 131 signal, we can resolve the changing of the phase factor  $\varphi$  between each modulation cycle and  
 132 find measurement linearity for the external field.

133 The measurement sequence we applied in the experiment is depicted in Fig. 1c, in which  
 134  $T_\phi$  is the field sensing time,  $T_{seq}$  is the sequence length of one measurement, and we use a  
 135 second measurement with the final pulse changed to  $(\pi/2)_{-x}$ . As a result, the fluorescence  
 136 signal is modulated with a frequency of  $f_s = 1/(2T_{seq})$ , which is also the sampling frequency  
 137 of the fluorescence readout. The demodulation of the fluorescence signal, denoted by *Demod.*  
 138 *1* in Fig. 1d, has a readout bandwidth  $f_s/2$  set by the Shannon sampling theorem. The  
 139 readout is further demodulated by another demodulator of the lock-in amplifier (LIA), de-  
 140 noted as *Demod. 2*. Upon measuring  $N$  samples of the fluorescence readout, the bandwidth  
 141 of the phase readout is narrowed down to  $f_s/(2N)$ . These measurements are schematically  
 142 shown in Fig. 1d.

143 The sensitivity of such measurements can be derived based on the fitting of the  $N$  samples  
 144 in the measurement time of  $N \cdot 2T_{seq}$ . The minimum detectable phase is derived as

$$\delta\phi = \frac{2}{\sqrt{N}} \frac{1}{C\sqrt{N}}, \quad (5)$$

145 where  $C$  is the fluorescence signal contrast,  $\mathcal{N}$  is the detected photon counts in each mea-  
 146 surement. The sensitivity to external magnetic field, however, is still subject to the applied  
 147 MW sequence, can be derived as

$$\eta = \frac{2}{\gamma_e |G(\omega)| C} \sqrt{\frac{2T_{seq}}{\mathcal{N}}}, \quad (6)$$

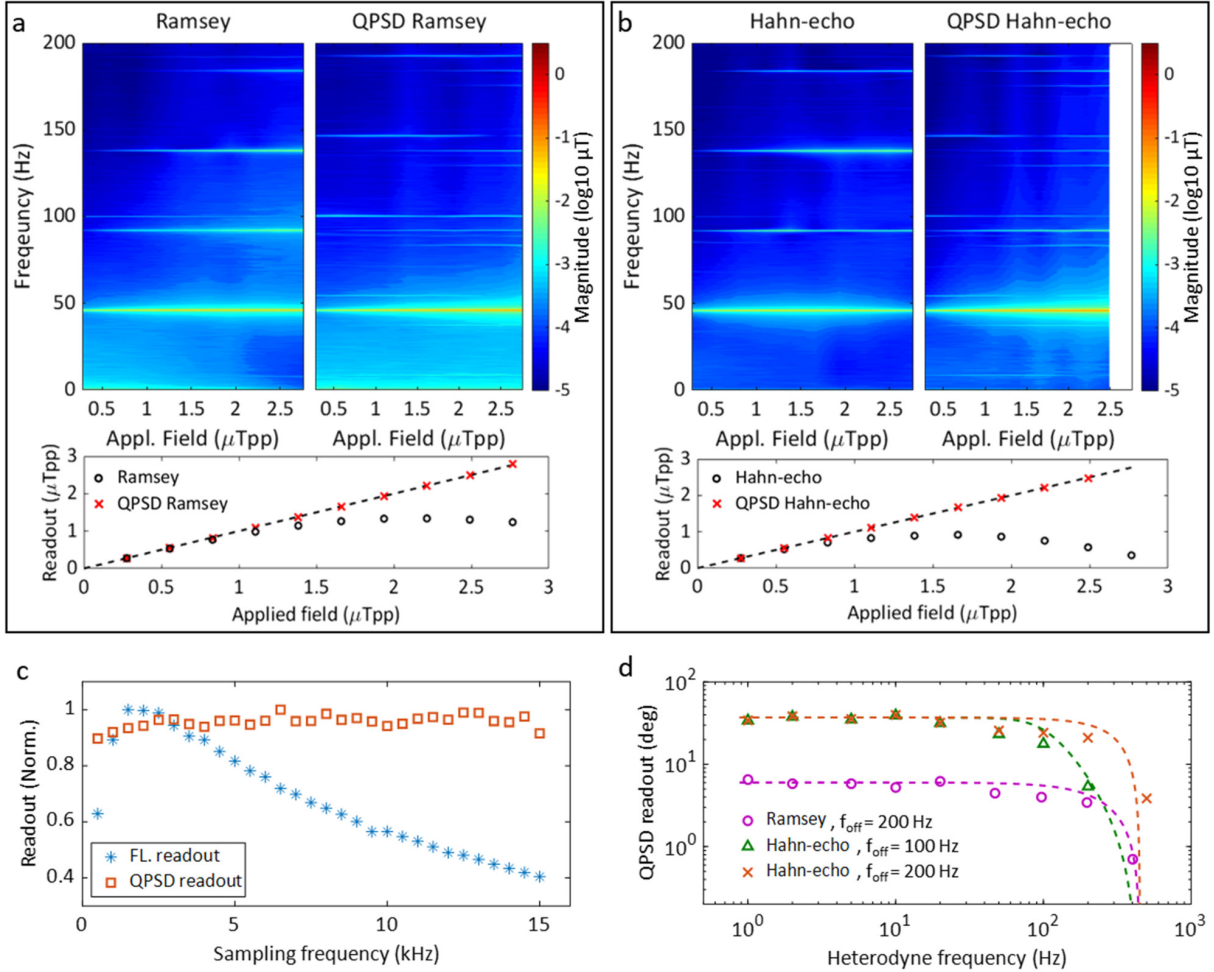


FIG. 2. Sensing performance of the QPSD. (a) Spectra and linearity comparison of the normal Ramsey readout and the QPSD readout. We apply  $T_\phi = 6.25\mu\text{s}$  in both measurements. The applied peak-to-peak field and the readout are plotted showing the linearity of the measurements. (b) Spectra and linearity comparison of normal Hahn-echo readout and the QPSD readout. The applied phase accumulation time  $T_\phi = 12.5\mu\text{s}$ . Thus, the Hahn-echo measurements performs a higher sensitivity but smaller dynamic range than the Ramsey measurements. (c) Signal response to different sampling frequencies. The measurements use the same calibration field, and the readouts are normalized to be plotted in the same vertical axis. (d) Measurement bandwidth. Ramsey and Hahn-echo sequences are applied to measure test fields at different frequencies with the same magnitude. The heterodyne frequency responses are limited in bandwidth by the cut-off frequency of the LIA.

148 where  $|G(\omega)|$  is the MW filter function which is usually used to describe the transfer function  
 149 of such a sensor from magnetic field to quantum phase. In comparison to the conventional  
 150 fluorescence readout, the sensitivity of QPSD readout deteriorates by a factor of  $\sqrt{2}$ . Details  
 151 about the sensitivity derivation can be seen in the Supplementary Materials (see Supple-  
 152 mentary Note 3).

153 In Fig. 2a and b, we compare the regular interferometry (single driving field) and with  
 154 the measurements obtained from the QPSD readout described above. The strength of the  
 155 applied external ac fields ranges from 0 to 3  $\mu\text{T}$ . For Ramsey measurements, the applied  
 156 fields are at a frequency of 46 Hz, and we use a field sensing time  $T_{\phi, \text{Ramsey}} = 6.25\mu\text{s}$ . For  
 157 Hahn-echo measurements, we use external fields at 80 kHz+46 Hz and the field sensing time  
 158  $T_{\phi, \text{Hahn}} = 2T_{\phi, \text{Ramsey}}$ . The test fields are sent to the diamond by a calibrated loop antenna.  
 159 The signal readout of the regular interferometry measurements is proportional to  $\sin(\phi)$ ,  
 160 where  $\phi \propto \gamma_e B$  is the accumulated quantum phase. The response is linear only when  $\phi$  is  
 161 small, limiting the dynamic range. Thus, the regular Ramsey and Hahn-echo readout quickly  
 162 saturate due to this limited LDR. We plot the Fourier transform of the readout signals also  
 163 in the figures. The harmonics of the 46 Hz signal rise significantly in the fluorescence readout  
 164 spectral due to the saturation induced by the limited LDR, compared to the QPSD readout  
 165 which shows the linearity over the entire field range. The high-order harmonics of the signal  
 166 detected by the QPSD readout are small and mainly arise from the function generator. In  
 167 the measurements, one could see the linewidth broadening induced by the increasing signal  
 168 power. The peak at 100 Hz, which is consistently seen in both the Ramsey and Hahn-echo  
 169 measurements, comes from the electronics instrumentation. Other side peaks seen near the  
 170 original signal frequency in the QPSD readout spectra are due to the mixing of the 100 Hz  
 171 power line harmonics and the 92 Hz signal harmonics in the LIA.

172 Besides the LDR, the method also demonstrates measurement robustness to changing  
 173 of  $T_{\text{seq}}$ . The motivation of using different  $T_{\text{seq}}$  is to get different sampling frequencies as  
 174 well as measurement bandwidth. Signal responses to different sampling frequencies, i.e.,  
 175 different  $1/2T_{\text{seq}}$ , are plotted in Fig. 2c. Characterized by the same test field, fluorescence  
 176 readout shows varying signal responses over the sampling frequency range, while the QPSD  
 177 readout almost stays at the same level because the measured phase factor only changes with  
 178 the external field and the sensing time  $T_{\phi}$ . It also indicates that the QPSD readout does  
 179 not change with varying of fluorescence signal contrast, which is affected by the low spin  
 180 polarization rate when  $T_{\text{seq}}$  is short in the regime of low excitation laser power.

181 The measurement bandwidth of the QPSD readout is shown in Fig. 2d, where the  
 182 signal responses to different test field frequencies are plotted. The plotted values are the  
 183 magnitudes at the corresponding frequencies in the Fourier transform of the QPSD readout.  
 184 For the measurements based on the Hahn-echo sequence, we detected the heterodyne signal

185 for the ac fields. The applied sequence length,  $T_{seq} = 100\mu s$ , gives the referencing frequency  
 186  $f_s = 5$  kHz for *Demod. 1*. We apply the second driving field with the frequency offset  
 187 at  $\delta f = 500$  Hz to have  $N = 10$  samples in a modulation cycle. Due to this, there will  
 188 be flexibility in deciding the single measurement bandwidth by setting the time constant  
 189 of *Demod. 2*. We choose different settings corresponding to the cut-off frequency of the  
 190 filter at 100 Hz and 200 Hz. Finally, one can conclude that the rotating frame modulation  
 191 provides QPSD readout magnetometry that has enhanced LDR and robustness in a flexible  
 192 bandwidth. As we show below, this can be used for measurement of arbitrary fields with  
 193 low distortion.

## 194 B. Frequency Offset Heterodyne Readout

195 Heterodyne readout has been used to improve the frequency resolution remarkably in  
 196 nuclear magnetic resonance spectroscopy. It is also a way to achieve high precision mi-  
 197 crowave sensing [34–36]. High-order dynamical decoupling sequences are used to narrow  
 198 the spectral linewidth by decoupling the sensor response from unwanted signal frequencies  
 199 [20, 21]. Here arises a trade-off between the measurable signal bandwidth and fidelity. High-  
 200 order dynamical decoupling can ensure a high sensitivity but only allows to measure signals  
 201 within the narrow bandwidth defined by the sequence. On the other hand, the lower limit  
 202 on the detectable signal frequency is set by the decoherence time of the sensor. Here, we  
 203 will use the Hahn-echo sequence in combination with the QPSD readout to measure signals  
 204 at frequencies that go beyond the coherence time of the sensor.

205 In Qdyne, the sampling time usually satisfies  $T_{seq} \neq mT_\phi$  so as to get the heterodyne  
 206 signal [21]. The frequency of this heterodyne signal depends on the timing offset. Here,  
 207 we choose the measurement sampling time  $T_{seq} = mT_\phi$  to obtain the heterodyne readout  
 208 depending on the signal frequency offset from  $1/T_\phi$ . As a result, the detected phase of signals  
 209 at frequencies of  $n/T_\phi$  is locked by the sequence, where  $n$  can be a random integer. On the  
 210 other hand, the frequency offset of signals can also introduce phase revivals, i.e. frequency  
 211 offset heterodyne signal, as shown in Fig. 3a. The detected heterodyne frequency would be  
 212 the exact offset of the signal frequency to  $1/T_\phi$ .

213 The frequency offset heterodyne readout is modeled based on the MW sequence filter  
 214 [37, 38]. Sampling happens in each time interval of  $[NmT_\phi, (Nm + 1)T_\phi]$ , where  $N \in \mathbb{Z}$ . For

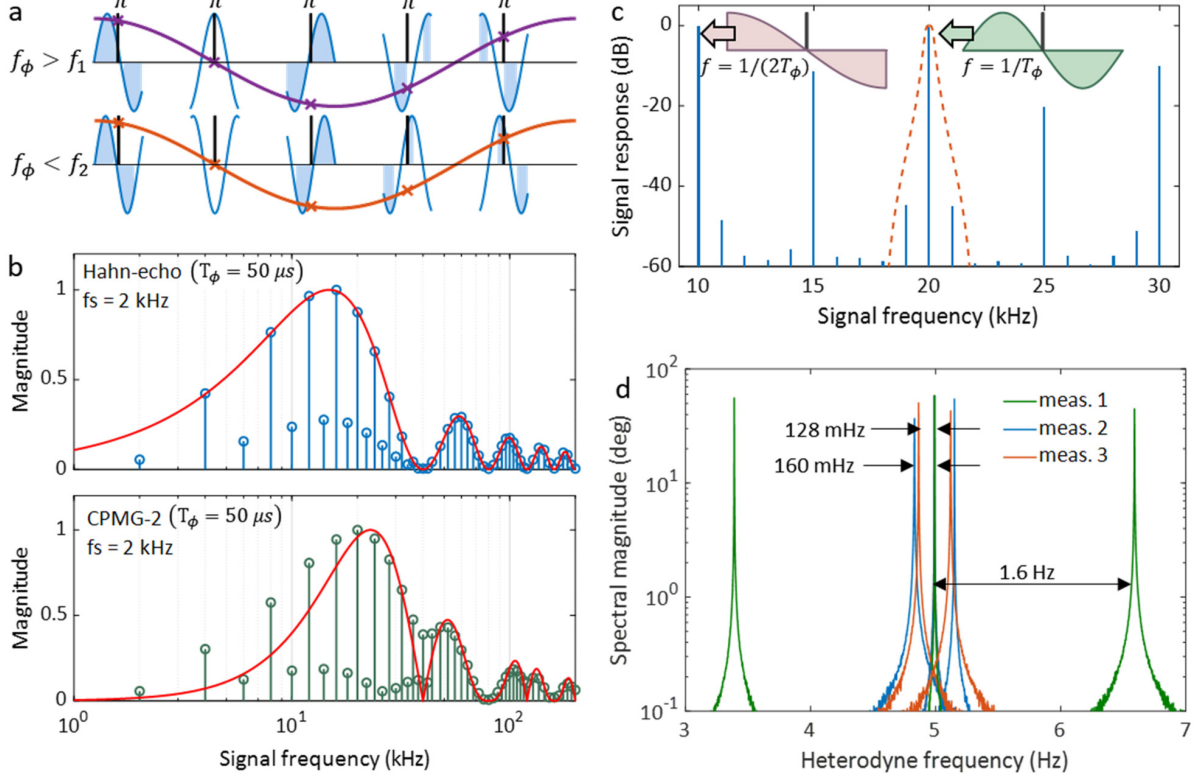


FIG. 3. Frequency Offset Heterodyne readout. (a) Hahn-echo sequence is used for this demonstration. The detected phase of the ac signal is locked by the sequence when the frequency is  $f_{ac} = f_\phi$ . Otherwise, a heterodyne signal of  $|f_{ac} - f_\phi|$  can be measured. The colored regions mark where the quantum phase is accumulated, while phase accumulations at the other areas are canceled in the spin evolution. The figure shows identical heterodyne signals due to  $f_\phi - f_1 = f_2 - f_\phi$ . (b) We apply ac fields at different frequencies with an offset of 5 Hz to the sensor so that 5 Hz peaks can be detected as the signal response. The signal frequency response of the Hahn-echo sequence and CPMG-2 sequence are plotted after normalization, respectively. In both measurements  $T_\phi = 50 \mu s$ , and the sampling frequency is 2 kHz according to the applied sequence length. The red lines are the filter functions in theory. (c) Signal frequency response of Hahn-echo measurements with  $1/T_{seq} = 10$  kHz. The dash line indicates the filter introduced by the lock-in amplifier. (d) Sequence dependency of the frequency resolution. In meas. 1, a 20.005 kHz field is applied and measured by sequences with  $T_\phi = 50 \mu s \pm 4 ns$ , and  $T_{seq} = 20T_\phi$ . In meas. 2, we keep  $T_\phi$  unchanged, and offset  $T_{seq}$  with  $\pm 4$  ns. In meas. 3, the frequency of the applied field is changed to 16.005 kHz while the other parameters are the same as meas. 2.

215 a random ac signal component  $B_{ac}(t) = B(\omega)e^{-i[\omega t + \varphi(\omega)]}$  and a measurement with the MW  
 216  $\pi$ -pulse number of  $n$ , we can get the accumulated quantum phase as (see Supplementary  
 217 Note 2)

$$\phi_r(N) = |G_n(\omega)| e^{i\left(-\frac{\omega T_\phi}{2} - \frac{P}{2}\pi\right)} \gamma_e B(\omega) e^{-i\varphi(\omega)} e^{-i\omega N m T_\phi}, \quad (7)$$

218 where  $N$  denotes the sampling timestamp,  $G_n(\omega) = |G_n(\omega)| e^{i\left(-\frac{\omega T_\phi}{2} - \frac{P}{2}\pi\right)}$  is the MW filter

219 function,  $P = 1$  when the  $\pi$ -pulse number  $n$  is odd and  $P = 2$  when  $n$  is even. Particularly,  
 220 when  $n = 1$  i.e. Hahn-echo sequence is applied, the filter function satisfies  $|G_1(2\pi/T_\phi)| =$   
 221  $|G_1(\pi/T_\phi)|$ . In principle, measurements of signals at a wide frequency range is feasible by  
 222 choosing the appropriate  $T_\phi$  in Hahn-echo measurements. For example, by using  $T_\phi < 1\mu\text{s}$ ,  
 223 one can achieve detection of signals at frequencies higher than 1 MHz. It is more challenging  
 224 to measure a signal at a lower frequency, such as a signal at 10 kHz, for the reason that a  
 225 longer  $T_2$  is required. With the property described above, it is feasible to use  $T_\phi = 50\mu\text{s}$   
 226 rather than  $T_\phi = 100\mu\text{s}$  to achieve the measurement with a better sensitivity due to the  
 227 higher signal contrast when  $T_\phi$  is smaller. For diamonds which have NV center ensembles  
 228 with  $T_2 < 100\mu\text{s}$ , the property makes it feasible to measure signals at the frequencies lower  
 229 than  $1/T_2$  beyond the coherence limit.

230 Given a reference frequency  $\omega_{ref} = k\omega_s, k \in \mathbb{N}$ , where  $\omega_s = 2\pi/(mT_\phi)$  and  $\omega \in$   
 231  $(\omega_{ref} - \omega_s/2, \omega_{ref} + \omega_s/2)$ , the evolving phase factor can be rewritten as  $e^{-i\omega NmT_\phi} =$   
 232  $e^{-i\omega_H t} \delta(t - NT_s)$ , where  $\omega_H = \omega - \omega_{ref}$  is the heterodyne frequency,  $\delta(t)$  is the Dirac  
 233 function, and  $T_s = mT_\phi$  is the sampling period. Thus, the readout signal turns to be

$$\phi_r(t) = G(\omega) \sum_{N=-\infty}^{\infty} \gamma_e B_H(t) \delta(t - NT_s), \quad (8)$$

234 where  $B_H(t) = B(\omega)e^{-i(\omega_H t + \varphi)}$  contains all the information from the origin signal to be  
 235 measured. As discussed in previous section, the quantum phase readout bandwidth is limited  
 236 by the cut-off frequency  $f_c$  of the filter of LIA. For any signal with a frequency range of  
 237  $[(k-1)f_s + f_c, (k+1)f_s - f_c]$ , aliasing can be filtered. Although a smaller  $f_c$  makes the  
 238 measurement bandwidth narrower, it ensures signals that in a larger frequency range can be  
 239 detected without aliasing. By changing  $T_\phi$  together with  $T_{seq}$ , we can resolve a spectrum in  
 240 multiple frequency bands with a series of sequences.

241 We present two specific examples of the measured frequency responses by using the Hahn-  
 242 echo and CPMG-2 sequence. We plot both the theoretical MW filter function and the  
 243 experimentally measured signal responses together in Fig. 3b. The field sensing time for  
 244 both experiment and theory calculations is set to be  $T_\phi = 50\mu\text{s}$ . In the experiments, we  
 245 measured the amplitudes of the frequency offset heterodyne signals with  $T_{seq} = 250\mu\text{s}$ , i.e.,  
 246 the magnetic field sampling rate is 4 kHz. Due to this reason, the measured MW filters are  
 247 combed with a frequency distance of 4 kHz. Aliasing signals exist between the main lobes

248 at a distance of 2 kHz, because the readout sampling frequency is  $f_s = 2$  kHz.

249 In order to measure signals that distribute in larger bandwidth, we can increase the  
 250 sampling frequency, for example, to  $f_s = 5$  kHz. The spectrum is plotted in Fig. 3c in  
 251 decibel, from which one can see that magnitudes are the same at 10 kHz and 20 kHz, i.e.,  
 252  $1/(2T_\phi)$  and  $1/T_\phi$  as discussed in the derivation. The insets of Fig. 3c depict the signals  
 253 that the quantum sensor detects during  $T_\phi$  at the two frequencies. In this measurement,  
 254 the bandwidth limited by the filter of the LIA is at 200 Hz, i.e., the single measurement  
 255 bandwidth is 400 Hz, and the detectable signal frequency range is 9600 Hz.

256 We notice that a single measurement cannot tell if the ac field frequency offset is positive  
 257 or negative from the heterodyne readout. Additional measurement is needed to distinguish  
 258 the direction of the frequency offset. By adding a difference to the phase accumulation  
 259 time  $T_\phi$  as well as the sequence time, we can change the reference frequency  $\omega_{ref}$  to get a  
 260 different heterodyne frequency. By seeing if the heterodyne frequency increases or decreases,  
 261 we can determine if the signal frequency is larger or smaller than the reference frequency.  
 262 As the measurements presented in Fig. 3d that  $T_\phi = 50\mu s$  is offset by a difference of 4  
 263 ns and  $T_{seq} = 10T_\phi$  changes accordingly, the detected heterodyne frequency of the signal  
 264 shift in two different directions. We further investigated the dependency of the heterodyne  
 265 frequency on the parameters by performing measurements that vary (i)  $T_{seq}$ , (ii)  $T_{seq}$  and  
 266  $\omega_{ref}$ . When  $T_\phi$  keeps unchanged, the heterodyne frequency shifts by

$$\Delta\omega_H = \omega_{ref}\Delta T_{seq}/T_{seq}. \quad (9)$$

267 Using the equation, we can estimate the frequency fidelity of the given sequence. For ex-  
 268 ample, with a timing error  $< 3$  ps, the frequency fidelity of a signal around 10 kHz could  
 269 be only 0.06 mHz. The frequency resolution can be arbitrarily high with a long  $T_{seq}$  at the  
 270 cost of bandwidth.

### 271 C. Sensing of Arbitrary Audio Signals

272 We demonstrate measurements of arbitrary audio signals by combining the QPSD readout  
 273 and the frequency offset heterodyne detection. We first generate a signal at 20.08 kHz with  
 274 its phase varying with time (see Fig. 4a). The MW filter is set by the Hahn-echo sequence

275 with  $T_\phi = 50\mu\text{s}$ . With the reference frequency is at 20 kHz, the heterodyne readout is at  
 276 80 Hz, as seen from the simulated curve. The phase of the external field is switched with  
 277 a cycle of 80 Hz and 40 Hz so that the experimental readout displays the phase change, as  
 278 shown in Fig. 4a.

279 Next, we apply a field with its frequency, amplitude and phase all arbitrarily changing.  
 280 The signal frequency is around 10 kHz and the signal bandwidth is within 400 Hz. Using

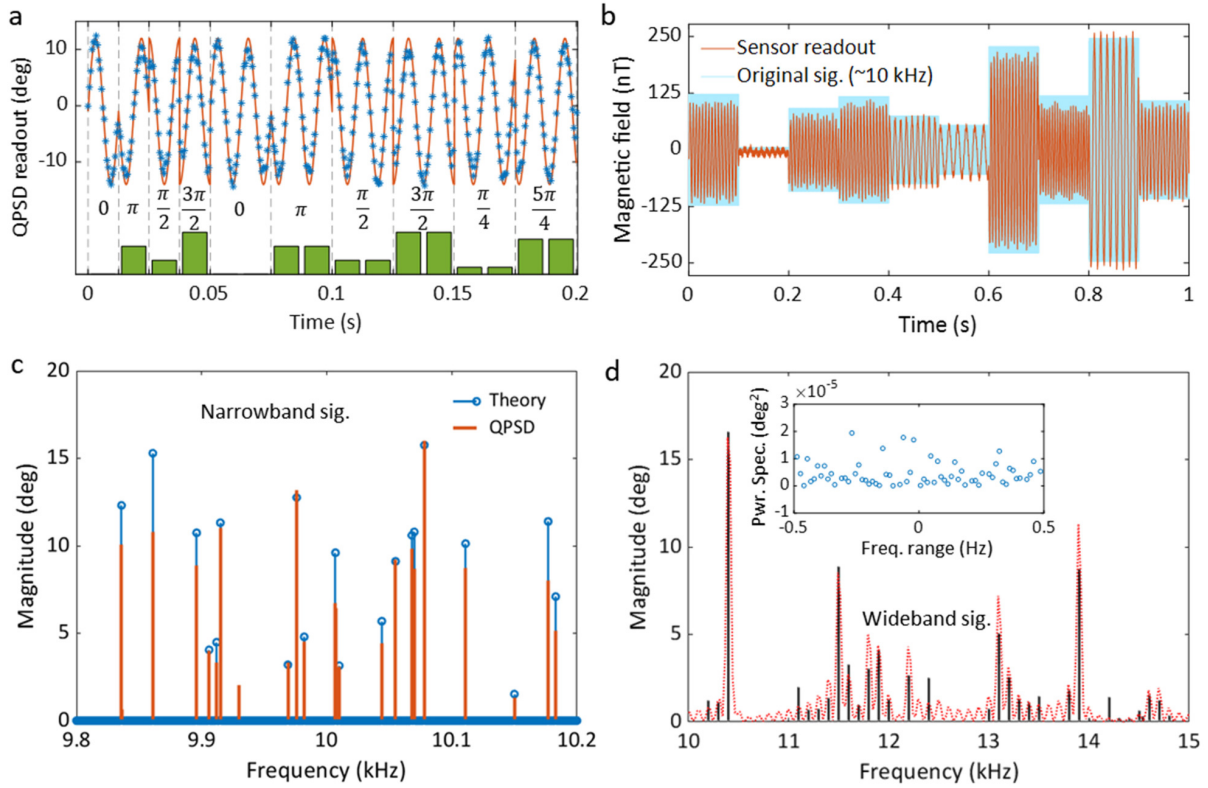


FIG. 4. Detection of arbitrary audio signals. (a) Phase response of the QPSD measurement. A 20.08 kHz signal with sequential phase changing is applied to the sensor. The bars show the phases at different time. Stars mark the readout of the sensor, and the curve is the simulated readout. (b) An ac field is applied with the frequency, amplitude and phase switched every 100 ms. The light blue areas corresponding to the right  $y$ -axis shows the applied field of around 10 kHz, and the red curve shows the QPSD readout. (c) Spectral comparison of the applied signal and the detected magnetic field in a narrow bandwidth. The applied signal is a sum of 20 different sine signals within 400 Hz bandwidth. (d) A signal with wide bandwidth between 10 to 15 kHz is applied and detected by varying the sequence. We set an 800 Hz bandwidth for the measurement of each sequence and use 6 measurements to cover the entire bandwidth. The red dash line shows the spectrum of the output of the AWG, and the solid black line is the spectrum of the detected magnetic field signal. The inset figure is the phase-noise power spectrum density plotted within 1 Hz bandwidth cut.

281  $1/T_{seq} = 10\text{kHz}$ , we can measure the signals close to 10 kHz with the same sensitivity as  
 282 the 20 kHz signal. The signal length is one second and consists of ten 100 ms parts. In Fig.  
 283 4b, both the applied field waveform and the QPSD readout are plotted. The heterodyne  
 284 frequencies well resolve the frequency differences in the original waveform. The amplitudes  
 285 of the readout also correspond to the applied field strength.

286 As discussed previously, the measurement bandwidth used in the experiment is 400 Hz.  
 287 For this, we perform a spectrum analysis as shown in Fig. 4c. The signal to be measured is  
 288 a sum of 20 tones with random frequencies, amplitudes and phases. In order to distinguish  
 289 the sign of frequency offsets for each component, we measure the signal using an alternative  
 290 sequence with  $T_\phi = 50\mu\text{s} + 2\text{ns}$ . The sharp peaks observed in the spectrum should shift  
 291 according to the changes of the measurement sequence, else we exclude them as noise signals  
 292 generated from our electronics. As shown in Fig. 4c, the applied frequencies are properly  
 293 resolved. Additionally, we find a 9.93 kHz noise spike from the environment. The errors in  
 294 magnitude of the measured signal could be induced by the LIA filter, as shown earlier in Fig.  
 295 2d. The errors could also be caused by an insufficient sampling number for demodulating  
 296 the rotating frame modulation. In the measurements, we apply sequences with their lengths  
 297 corresponding to a sampling frequency  $f_s = 5\text{kHz}$ . The frequency difference of the two MWs  
 298 is  $\delta f = 500\text{ Hz}$  and  $N = 10$  for reading out a phase sample. To increase the measurement  
 299 precision, if we use a smaller  $\delta f$ , it will decrease the bandwidth.

300 Though the bandwidth of each measurement sequence is limited, we can still measure  
 301 a signal with a wider bandwidth by merging several measurements. The condition is that  
 302 the signal bandwidth should not be larger than the sampling frequency to avoid frequency  
 303 aliasing. In Fig. 4d, we perform a spectrum analysis for a signal within a bandwidth  
 304 from 10 kHz to 15 kHz. The signal to be detected is a sum of 10 components with their  
 305 frequencies randomly distributed in the bandwidth. The signal is generated by an arbitrary  
 306 signal generator (AWG) and sent to the test field coil. The dotted curve in the figure  
 307 displays the spectrum of the electrical signal from the AWG. There are some harmonics  
 308 near each main component due to the limited AWG internal clock and signal length. The  
 309 components at different frequencies are measured by varying  $T_\phi$  to get different referencing  
 310 frequencies for heterodyne detection. The inset figure shows the power spectrum of the  
 311 QPSD readout noise within 1 Hz bandwidth, from which we calculate the square root of  
 312 the standard deviation  $\sigma_{phase} = 0.0022^\circ$ . The magnetic field sensitivity depends on the

313 applied sequence and the corresponding frequency response. In the case of the Hahn-echo  
 314 sequence with  $T_\phi = 50\mu\text{s}$ , we have a calibrated scalar factor of  $k_{sf} = 0.071^\circ/\text{nT}$ , and the  
 315 magnetic field sensitivity is  $\eta = 31\text{pT}/\sqrt{\text{Hz}}$ . Taking the scalar factor into the calculation  
 316 of LDR  $[-\pi, \pi]$ , we can get the dynamic range in decibels as  $20 \log[\pi/(k_{sf}\eta)] = 98\text{dB}$ . The  
 317 sensitivity can be further optimized by, e.g., using higher laser power, applying high-order  
 318 dynamical decoupling sequences, and implementing flux concentration.

319 Finally, we demonstrate the detection and demodulation of audio signals. Although 10  
 320 kHz is within the audio frequency band, most of the daily audio sounds have frequencies  
 321 ranging from hundreds of Hz to a few kHz. Therefore, signals need to be modulated to a  
 322 detectable frequency range. For this, we have used (i) a melody piece composed of 3 tones  
 323 and (ii) a small part from Dr. Martin Luther King Jr.'s famous speech "I have a dream", to  
 324 test the waveform reconstruction by the diamond quantum sensor. The tones of the melody  
 325 have frequencies distributed between 500 Hz and 700 Hz. Therefore, we mix it with a 9.5  
 326 kHz reference to get the signal modulated around 10 kHz and broadcast the mixed signal to  
 327 the diamond. For case (ii), we have to compress the signal bandwidth into 200 Hz and then  
 328 modulate it with a 10 kHz reference. The audio reconstructed from the diamond sensor can  
 329 be heard and compared with the original audio (see Supplementary Audio S1-S4).

### 330 III. DISCUSSIONS

331 In this work, we overcome the LDR limitation of the conventional interferometric readout  
 332 through a new technique that includes the QPSD scheme and the frequency offset heterodyne  
 333 readout. The technique allows one to measure unknown signals with maximal sensitivity  
 334 independent of their dynamic range. It improves the feasibility for quantum sensors to  
 335 perform high-sensitive measurements of different physical quantities using interferometric  
 336 methods, beyond magnetometry.

337 Theoretically, the extended LDR comes from the multiple measurements that have the  
 338 quantum phase evolving through the entire phase range  $[-\pi, \pi]$  so that the initial phase  
 339 factor that contains the external field information can be resolved. Such an extended phase  
 340 range affects the measurement bandwidth as well as the sensitivity. In theory, the sensi-  
 341 tivity does not deteriorate a lot from the conventional fluorescence readout except for a  
 342 factor of  $\sqrt{2}$ . While in the experiment, we suffer from a low contrast  $C = 0.19\%$  due to

343 the low excitation laser power (80 mW). The contrast and the fluorescence photon count  
344 can significantly increase when the laser reaches saturation power [39]. Different dynamical  
345 decoupling sequences can also improve the magnetic field sensitivity through the filter func-  
346 tion  $G(\omega)$ . Flux concentration could further improve the signal-noise ratio [31, 40]. The flux  
347 concentrator can be very small compared to conventional dipole antennas because the gain  
348 no longer depends on the signal wavelength. With the millimeter size diamond dimension,  
349 the flux concentration factor can easily reach a factor of hundreds when using a concentrator  
350 in centimeters.

351 The QPSD readout can also enhance the capability of vector magnetometry. Convention-  
352 ally, fluorescence emitted from NV centers in multiple orientations is measured sequentially  
353 to acquire the vector components. Similar to the methods developed here, one could also  
354 modulate the signal on each orientation with different modulation frequencies [41]. Per-  
355 forming measurements on different NV orientations with appropriate synchronization can  
356 suppress the phase errors in vector reconstruction.

357 In conclusion, we demonstrated high-sensitive distortion-free quantum-assisted detection  
358 of audio signals, including melody and speech, using the QPSD scheme in combination with  
359 the heterodyne readout. A further improvement in sensitivity can be achieved by using  
360 flux concentrators. One could also generalize the current methods to achieve vector magne-  
361 tometry with extended LDR. We envisage that the techniques developed here will have the  
362 potential to develop low-distortion, small-volume quantum sensors for various applications  
363 in science and technology.

## 364 IV. METHODS

### 365 A. Experimental setup

366 The diamond used in the experiment is a (111)-oriented  $(0.5 \text{ mm})^3$  cube obtained from a  
367 single crystal grown by the temperature gradient method at high-pressure high-temperature  
368 (HPHT) conditions. The diamond is 99.97%  $^{12}\text{C}$  enriched, and has an initial nitrogen con-  
369 centration of 1.4 ppm. The final NV concentration is 0.4 ppm after electron irradiation  
370 and annealing. Dephasing time of the NV ensemble is obtained as  $T_2^* = 8.5 \mu\text{s}$  by Ramsey  
371 sequence, and a decoherence time  $T_2 = 200 \mu\text{s}$  is measured by Hahn-echo sequence. The dia-

372 mond is positioned at center of a home-built three dimension coils system, and is illuminated  
 373 by a 532 nm laser (Lighthous Sprout-G) at around 80 mW. Microwave signals are generated  
 374 from two sources (Rohde&Schwarz, SMIQ03B) and are individually cut by two switches  
 375 before the combination. Measurement sequences are generated by a data timing generator  
 376 (Tekreonix, DTG5274). After the combination and amplification of the MW signals, MW  
 377 pulses are feed to the diamond through a dielectric resonator antenna [42]. The detected  
 378 fluorescence signal is demodulated by a LIA (Zurich Instruments, HF2LI) which has two  
 379 independent differential input channels and demodulators. To generate arbitrary magnetic  
 380 fields, we write signals to an AWG (Tektronix, AWG520) with  $10^5$  samples per second out-  
 381 put sampling rate. The test signals are continuously repeated and sent to a copper loop  
 382 near the diamond.

## 383 B. Spectrum analyzing

384 The spectrum to be analyzed is divided into several sections with the bandwidth set  
 385 by the LIA for data acquisition. In each section, the center frequency determines  $T_\phi$  of  
 386 the measurement sequence. Usually, the center frequency satisfies  $f_c = 1/T_\phi + \varepsilon/T_{seq}$ ,  
 387 where  $\varepsilon = 0, \pm 1$ . A time trace is recorded after running the sequence, and a spectrum is  
 388 acquired from the Fourier transform of the time trace. However, the spectrum is a fold of  
 389 the two sidebands with respect to the center frequency. The sequence with  $T'_\phi = T_\phi + t_{clk}$   
 390 and  $T'_{seq} = mT'_\phi$  is applied to get an alternate spectrum with analyzed frequencies shift by  
 391  $\Delta f = \pm |1/T_\phi - 1/T'_\phi|$ . The direction of the frequency shift shows which side the signal  
 392 component belongs to. In the algorithm, we set a threshold to separate signal spikes from  
 393 noise, and use the known sequences induced spectrum frequency shift to distinguish the signs  
 394 of the signal offset frequency to the center frequency. The signal spikes that do not shift  
 395 according  $\Delta f$  are recognized as systematic noise spikes. Then, the spectrum of the selected  
 396 section can be replotted as the example shown in Fig. 4c. After measuring the spectra of  
 397 all the sections, we can get the final spectrum by merging them together.

398 **V. ACKNOWLEDGMENTS**

399 We acknowledge financial support by European Union’s Horizon 2020 research and inno-  
400 vation program ASTERIQS under grant No. 820394, European Research Council advanced  
401 grant No. 742610, SMel, Federal Ministry of Education and Research (BMBF) project  
402 MiLiQuant and Quamapolis, German Research Foundation grant GRK 2198 and 2642, and  
403 Japan Society for the Promotion of Science (JSPS) KAKENHI No. 17H02751.

- 
- 404 [1] Gustavson, T. L., Bouyer, P. & Kasevich, M. A. Precision rotation measurements with an  
405 atom interferometer gyroscope. *Phys. Rev. Lett.* **78**, 2046 (1997).
- 406 [2] Allred, J. C., Lyman, R. N., Kornack, T. W. & Romalis, M. V. High-sensitivity atomic  
407 magnetometer unaffected by spin-exchange relaxation. *Phys. Rev. Lett.* **89**, 130801 (2002).
- 408 [3] Hinkley, N. *et al.* An atomic clock with 10–18 instability. *Science* **341**, 1215–1218 (2013).
- 409 [4] Kominis, I. K., Kornack, T. W., Allred, J. C. & Romalis, M. V. A subfemtotesla multichannel  
410 atomic magnetometer. *Nature* **422**, 596–599 (2003).
- 411 [5] Kornack, T. W., Ghosh, R. K. & Romalis, M. V. Nuclear spin gyroscope based on an atomic  
412 comagnetometer. *Phys. Rev. Lett.* **95**, 230801 (2005).
- 413 [6] Kitching, J., Knappe, S. & Donley, E. Atomic sensors—a review. *IEEE Sens. J* **11**, 1749–1758  
414 (2011).
- 415 [7] Barry, J. F. *et al.* Sensitivity optimization for nv-diamond magnetometry. *Rev. Mod. Phys.*  
416 **92**, 015004 (2020).
- 417 [8] Shah, V., Vasilakis, G. & Romalis, M. V. High bandwidth atomic magnetometry with  
418 continuous quantum nondemolition measurements. *Phys. Rev. Lett.* **104** (2010).
- 419 [9] Taylor, J. M. *et al.* High-sensitivity diamond magnetometer with nanoscale resolution. *Nat.*  
420 *Phys.* **4**, 810–816 (2008).
- 421 [10] Neumann, P. *et al.* High-precision nanoscale temperature sensing using single defects in  
422 diamond. *Nano Lett.* **13**, 2738–2742 (2013).
- 423 [11] Michl, J. *et al.* Robust and accurate electric field sensing with solid state spin ensembles.  
424 *Nano Lett.* **19**, 4904–4910 (2019).

- 425 [12] Chen, E. H. *et al.* High-sensitivity spin-based electrometry with an ensemble of nitrogen-  
426 vacancy centers in diamond. *Physical Review A* **95**, 053417 (2017).
- 427 [13] Tisler, J. *et al.* Single defect center scanning near-field optical microscopy on graphene. *Nano*  
428 *Lett.* **13**, 3152–3156 (2013).
- 429 [14] Zheng, H. J. *et al.* Zero-field magnetometry based on nitrogen-vacancy ensembles in diamond.  
430 *Phys. Rev. Appl.* **11** (2019).
- 431 [15] Wickenbrock, A. *et al.* Microwave-free magnetometry with nitrogen-vacancy centers in dia-  
432 mond. *Appl. Phys. Lett.* **109** (2016).
- 433 [16] Barry, J. F. *et al.* Optical magnetic detection of single-neuron action potentials using quantum  
434 defects in diamond. *Proc. Nat. Acad. Sci.* 201601513 (2016).
- 435 [17] Wang, P. *et al.* High-resolution vector microwave magnetometry based on solid-state spins in  
436 diamond. *Nat. Commun.* **6**, 6631 (2015).
- 437 [18] Farfurnik, D. *et al.* Optimizing a dynamical decoupling protocol for solid-state electronic spin  
438 ensembles in diamond. *Phys. Rev. B* **92** (2015).
- 439 [19] de Lange, G., Riste, D., Dobrovitski, V. V. & Hanson, R. Single-spin magnetometry with  
440 multipulse sensing sequences. *Phys. Rev. Lett.* **106** (2011).
- 441 [20] Schmitt, S. *et al.* Submillihertz magnetic spectroscopy performed with a nanoscale quantum  
442 sensor. *Science* **356**, 832–836 (2017).
- 443 [21] Boss, J. M., Cujia, K. S., Zopes, J. & Degen, C. L. Quantum sensing with arbitrary frequency  
444 resolution. *Science* **356**, 837–840 (2017).
- 445 [22] Clevenson, H. *et al.* Robust high-dynamic-range vector magnetometry with nitrogen-vacancy  
446 centers in diamond. *Appl. Phys. Lett.* **112**.
- 447 [23] Nusran, N. M., Momeen, M. U. & Dutt, M. V. G. High-dynamic-range magnetometry with a  
448 single electronic spin in diamond. *Nat. Nano.* **7**, 109–113 (2012).
- 449 [24] Joas, T. *et al.* Online adaptive quantum characterization of a nuclear spin. *Npj Quantum Inf.*  
450 **7**, 1–8 (2021).
- 451 [25] Gurses, B. V., Whitmore, K. T. & Cohen, M. B. Ultra-sensitive broadband ”awesome” electric  
452 field receiver for nanovolt low-frequency signals. *Rev. Sci. Instrum.* **92** (2021).
- 453 [26] Cohen, M. B. *et al.* Broadband longwave radio remote sensing instrumentation. *Rev. Sci.*  
454 *Instrum.* **89** (2018).

- 455 [27] Sedlacek, J. A. *et al.* Microwave electrometry with rydberg atoms in a vapour cell using bright  
456 atomic resonances. *Nat. Phys.* **8**, 819–824 (2012).
- 457 [28] Meyer, D. H., Kunz, P. D. & Cox, K. C. Waveguide-coupled rydberg spectrum analyzer from  
458 0 to 20 ghz. *Phys. Rev. Appl.* **15** (2021).
- 459 [29] Boto, E. *et al.* Moving magnetoencephalography towards real-world applications with a wear-  
460 able system. *Nature* **555**, 657 (2018).
- 461 [30] Gerginov, V., da Silva, F. C. S. & Howe, D. Prospects for magnetic field communications and  
462 location using quantum sensors. *Rev. Sci. Instrum.* **88** (2017).
- 463 [31] Fescenko, I. *et al.* Diamond magnetometer enhanced by ferrite flux concentrators. *Phys. Rev.*  
464 *Res.* **2** (2020).
- 465 [32] Seidel, D. & Muga, J. G. Two-frequency ramsey interferometry. *Phys. Rev. A* **75** (2007).
- 466 [33] Vutha, A. C. & Hessels, E. A. Frequency-offset separated oscillatory fields. *Phys. Rev. A* **92**  
467 (2015).
- 468 [34] Meinel, J. *et al.* Heterodyne sensing of microwaves with a quantum sensor. *Nat. Commun.*  
469 **12**, 2737 (2021).
- 470 [35] Chu, Y. M. *et al.* Precise spectroscopy of high-frequency oscillating fields with a single-qubit  
471 sensor. *Phys. Rev. Appl.* **15** (2021).
- 472 [36] Staudenmaier, N., Schmitt, S., McGuinness, L. P. & Jelezko, F. Phase-sensitive quantum  
473 spectroscopy with high-frequency resolution. *Phys. Rev. A* **104** (2021).
- 474 [37] Staudacher, T. *et al.* Nuclear magnetic resonance spectroscopy on a (5-nanometer)<sup>3</sup> sample  
475 volume. *Science* **339**, 561–563 (2013).
- 476 [38] Bar-Gill, N., Pham, L. M., Jarmola, A., Budker, D. & Walsworth, R. L. Solid-state electronic  
477 spin coherence time approaching one second. *Nat. Commun.* **4**, 1743 (2013).
- 478 [39] Zhang, C. *et al.* Diamond magnetometry and gradiometry towards subpicotesla dc field mea-  
479 surement. *Phys. Rev. Appl.* **15** (2021).
- 480 [40] Griffith, W. C., Jimenez-Martinez, R., Shah, V., Knappe, S. & Kitching, J. Miniature atomic  
481 magnetometer integrated with flux concentrators. *Appl. Phys. Lett.* **94**, 023502 (2009).
- 482 [41] Schloss, J. M., Barry, J. F., Turner, M. J. & Walsworth, R. L. Simultaneous broadband vector  
483 magnetometry using solid-state spins. *Phys. Rev. Appl.* **10** (2018).
- 484 [42] Kapitanova, P. *et al.* 3d uniform manipulation of nv centers in diamond using a dielectric  
485 resonator antenna. *Jetp Lett.* **108**, 588–595 (2018).

## Supplementary Files

This is a list of supplementary files associated with this preprint. Click to download.

- [SupplementaryInformation.docx](#)
- [AudioS1melody.wav](#)
- [AudioS2detmelody.wav](#)
- [AudioS3voice.wav](#)
- [AudioS4detvoice.wav](#)